Printed Electronics for space applications: an approach towards the integration of passive electronics

6th Space Passive Component Days (SPCD), International Symposium

13-16 October 2026
ESA/ESTEC, Noordwijk, The Netherlands

Miren Hayet Otero[(1) (2)], Julen Caballero Anton[(1) (2)], Leire Bilbao Alba[(1)], Ana Perez Marquez[(1)], Olatz Adarraga[(1)], Ibai Santamaría[(1)], Izaskun Bustero[(1)], Jose Manuel Gonzalez[(2)]

[(1)] Tecnalia Research & Innovation
Mikeletegi Pasealekua, 2
E-20009 Donostia-San Sebastián, Gipuzkoa (Spain)
Email: miren.hayet@tecnalia.com

[(2)] Department of Electronic Technology - Faculty of Engineering of Vitoria-Gasteiz
University of the Basque Country (EHU)01006 Vitoria-Gasteiz, Araba (Spain)
Email: josemanuel.gonzalezp@ehu.eus

INTRODUCTION

Functional printing or Printed Electronics (PE) is defined as the controlled deposition of advanced materials onto a surface with the objective of endowing the resulting object with active or intelligent properties. This approach enables the integration of specific functionalities that depend both on the intrinsic nature of the material, and the design of the printed pattern [1]. The materials utilized, typically in the form of functional inks, feature carefully tailored compositions ranging from systems with electrical properties (conductive, resistive, or dielectric) to stimuli-responsive materials capable of reacting to external triggers, such as variations in temperature, pressure, or chemical and biological interactions.

From a processing perspective, PE is characterized as an automated, additive methodology. This stands in stark contrast to conventional electronics, which rely predominantly on subtractive technologies such as photolithography, chemical etching, and lift-off processes [2]. These traditional approaches necessitate multiple complex stages and the intensive use of corrosive chemicals, resulting in a significant environmental footprint. Consequently, printed electronics, by leveraging additive manufacturing principles, emerge as a more sustainable alternative by substantially reducing both raw material consumption and waste generation.

Additionally, functional printing allows for multilayer processing, making it possible to manufacture full devices with electronics embedded directly within the part. Unlike traditional methods, which separate structural fabrication from functionalization and require post-process assembly, functional printing integrates both into a unified workflow. This capability allows for greater integration, enables new architectures that are impossible to achieve with conventional techniques, and reduces overall weight, volume, and manufacturing costs [3].

The deposition process constitutes a key element of functional printing, employing various technologies such as inkjet, aerosol jet, screen printing, and multi-material 3D printing. These techniques allow for high-precision control over both the geometry and the distribution of the functional material on the substrate. Among these, screen printing stands out as a mature, robust, and highly scalable technology, widely adopted in industrial settings for the repeatable fabrication of functional patterns [1]. Its operating principle is based on the transfer of ink through a mesh using a squeegee, where a mask defines the printing regions; this makes it particularly suitable for mass production and large-area applications. In contrast, piezojet, a piezoelectric-based inkjet technology, enables the non-contact deposition of ink micro-droplets with a high degree of resolution and control. In this process, a piezoelectric actuator generates pressure pulses that expel controlled volumes of droplets from the nozzle, facilitating the direct printing of fine and complex patterns without the need for masks. This technique is especially appropriate for applications requiring high precision, low material consumption, and selective deposition on sensitive or non-planar substrates [4].

In the context of multifunctional composites and Structural Health Monitoring (SHM) PE arises as a promising technique for the integration of electronic functionalities. It has been demonstrated that, in contrast to physical components, printed patterns do not generate discontinuities and structural properties of composites do not deteriorate [5]. On the other hand, Additive Manufacturing Electronics (AME) is based on the sequential combination of conventional additive manufacturing processes -such as Fused Filament Fabrication (FFF) or Stereolithography (SLA)- with PE techniques. AME has recently emerged as a promising route for implementing electronic components with reduced cost, rapid prototyping, and unprecedented geometric freedom compared to conventional printed circuit board (PCB) technology [6].

This paper presents four representative use cases that illustrate the potential of functional printing for passive components in space applications. The development of a helical antenna for satellite-to-ground communications operating in the ISM band is presented, demonstrating how the combination of Fused Deposition Modelling (FDM) and PiezoJet technologies allows for the integration of complex geometries with a performance of nearly 4 dB of gain. The manufacturing of a coplanar waveguide (CPW) filter based on metamaterial-inspired resonators via AME is also explored. Concerning multifunctional composites, nanofiber-veil-allowed integration of thermal and mechanical sensing capabilities into Carbon Fiber Reinforced Polymer Composite (CFRPC) material is presented. The resulting system withstands autoclave curing and offers a linear response with a thermal sensitivity of 0.5 Ω/°C and calibration factors between 1.6 and 1.7, ensuring accurate measurements of temperature and strain. Finally, a surface temperature control system consisting of a screen-printed silver-based heater and thermistor embedded into CFRPC is presented.

AME ANTENNA FOR ISM BAND

In this section a novel AME helical antenna operating in the 2.9 GHz Telemetri band is presented. The objective of this study is to fabricate a fully printed antenna that can support satellite-to-ground communications. To this end, the recommended gain is between 0 and 10 dBi. As most of the power required for communication is applied at ground stations, leaving minimal work to be done in orbit, a target gain of 3 dBi has been set.

The primary design challenges consist of adjusting the antenna size to achieve the correct frequency resonance and ensuring that the fabricated prototype is consistent with these results, despite the imperfections caused by additive manufacturing methods. Simulations in HFSS software were employed to optimize the design in accordance with the specified material properties and overall conditions, allowing for the identification of the optimal design configuration. The antenna exhibits a gain close to 4 dBi at a frequency of 2.9 GHz. The proposed design offers considerable potential for integration into space communications.

Design and Simulation

The design consists of a printed conductor wound into a cylinder following a helix geometry (Fig. 1).

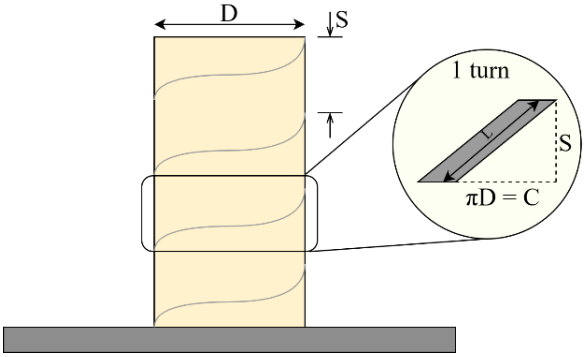


Fig. 1. Model and relevant design parameters for an helical antenna.

The antenna geometry calculations were performed using Kraus equations [7]. A critical parameter in the design is the antenna circumference *C*; it must be like the wavelength of the target frequency λ as described by (1).

$$0.8\lambda \lesssim C \lesssim 1.2\lambda, C = 2\pi r \quad (1)$$

The number of turns affects the gain, along with the ground plane size. To adjust the electrical length of the antenna, permittivity measurements were taken in the dielectric material to select the fill factor of the cylinder structure. Equation

(2) shows the relation between one turn wire length L, the separation between turns S and the circumference of one turn around the cylinder C. These variables can be observed in Fig. 1.

$$L = \sqrt{C^2 + S^2}, \tan \alpha = \frac{S}{C} \tag{2}$$

Materials and Methods

The manufacture of the antenna using printing techniques involves several steps, carried out using FDM and PiezoJet printing processes. Fig. 2 illustrates the antenna manufacturing process. The steps associated with each image are listed below in the corresponding order:

a) The polycarbonate (PoliMAX TOUGH PC) support for the antenna and the ground plane are printed using FDM.
b) The surface of the cylinder and the mass plane are sanded to remove irregularities and smooth the surface.
c) The ground plane is painted with silver ink, and the SMA connector is attached with conductive and mechanical adhesive to the backside of the plane.
d) Finally, the helical antenna is printed of WIK 20487-36A silver ink using PiezoJet technology mounted in a 5 axis CNC machine.

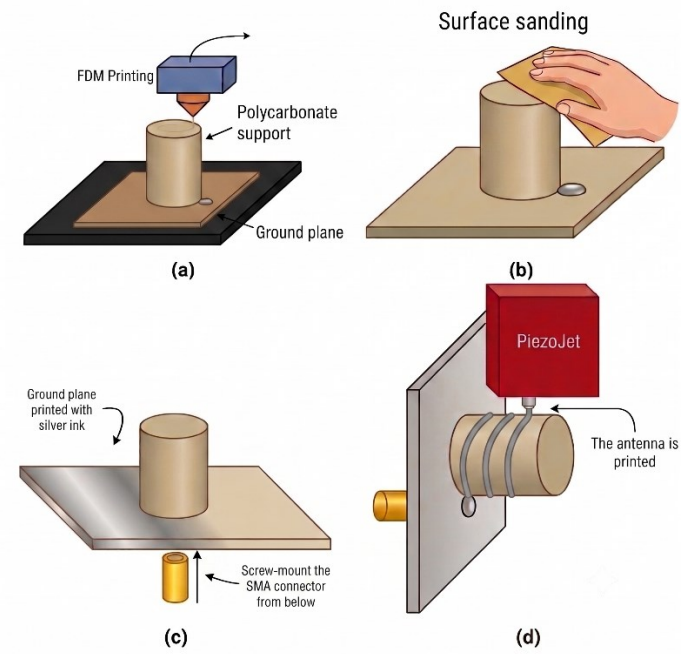


Fig. 2. Fabrication process of AME helical antenna: (a) antenna support printing via FDM; (b) surface sanding; (c) connector and ground plane connection; (d) antenna printing via PiezoJet.

Results and Discussion

The measurements were performed by placing two antennas connected to a VNA face to face. The reference antenna is a Deepace UWB with a gain of 3 dB across the entire measurement spectrum. Knowing this, by facing both antennas and measuring the S-parameters, the manufactured gain can be obtained using Friss's equations shown in (3) where P_r is the received power (W), P_t is the transmitter input power (W), G_t is the isotropic power gain of the transmitting antenna, G_r is the isotropic power gain of the receiving antenna, λ is the wavelength of the carrier frequency (m), and d is the distance between the transmitter and receiver antennas (m) [8].

$$P_r = P_t G_t G_r \left(\frac{\lambda}{4\pi d}\right) \tag{3}$$

Fig. 3 shows the S_{11} graph of the measured values against those obtained in simulation. It can be observed that, at a frequency of 2.9GHz, resonance occurs in both, the simulation and the measurement, with a little shift in the simulation.

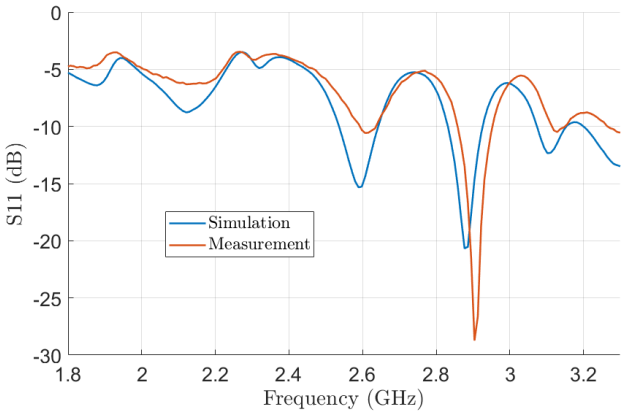


Fig. 3. Simulated and measured S-parameters of AME helical antenna.

Fig. 4 shows the radiation pattern of the measured gain. The directivity angle (HPBW) is approximately 21º, which classifies it the antenna as directional. The peak gain has a value of almost 4dBi which exceeds the target value and therefore meets the criteria. A null value appears close to 300º, which is probably due to an error during the measurement.

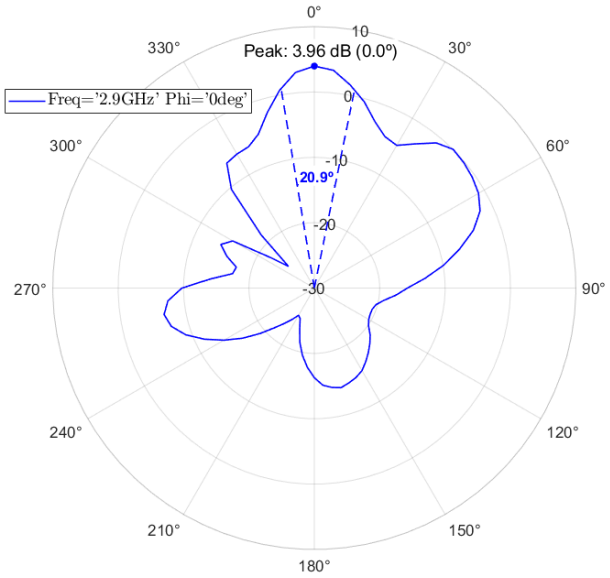


Fig. 4. Measured gain of AME helical antenna.

Conclusion

A 2.9 GHz helical antenna has been successfully designed, fabricated and characterized using additive manufacturing techniques, The fabricated antenna achieved a gain close to 4 dBi with a directivity angle (HPBW) of approximately 21º, demonstrating directional characteristics. This design offers advantages such as integrability within space applications through additive manufacturing methods. The following conclusions may be drawn:

- The integration of PiezoJet technology for printing the helical structure combined with FDM for structural components presents novel manufacturing capabilities for complex antenna geometries.
- The proposed design strikes a balance between manufacturing simplicity, antenna efficiency, and the ability to achieve consistent results despite AM process variations.

This work represents a significant advancement in the development of additively manufactured antennas for space communication applications. Also, it demonstrates that there is potential for further optimization using advanced materials such as ULTEM to improve thermal resistance for harsh space environments.

AME FILTER

Filters based on CPW technology and metamaterial-inspired resonators were presented as a planar alternative for the miniaturization of microwave filters [9]. Specifically, multiple tuned split-ring resonators (SRRs)-loaded CPW enable deep and controllable stop bands in an electrically compact footprint. AME-enabled geometric freedom allows for the manufacturing of new filter topologies such as stacked/embedded resonator networks in printed dielectric volumes which remain unexplored. This section presents a preliminary analysis for the feasibility of an AME CPW filter printed on space-validated substrate.

Design and Simulations

The design considered for analysis is a stopband filter consisting of a CPW transmission line loaded with six SRRs, whose centres are aligned with the gaps of the transmission line. Fig. 5 shows a model of the analyzed design with the relevant dimensions.

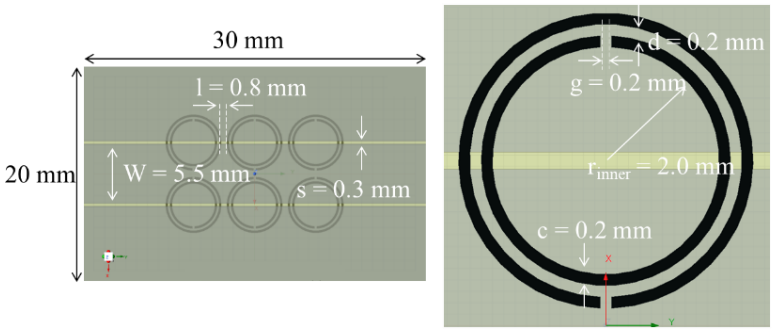


Table 1: Dimensions of the design parameters of AME CPW stopband filter

d (µm)	200	**R_{in} (mm)**	2
c_{in} (µm)	200	**W (mm)**	5.5
c_{out} (µm)	200	**s_1 (mm)**	0.3
g_{in} (µm)	200	**s_2 (mm)**	0.3
g_{out} (µm)	200		

Fig. 5. Design layout of stopband CPW filters.

The selected material for the substrate manufacturing is ThermaX PEI filament made from Ultem 9085 resin (ε_r = 3.0 – 3.2, $tan\delta$ = 0.0026 – 0.0027) [10]. The design has been simulated in a substrate with permittivity value of ε_r = 3.0, loss tangent of $tan\delta$ = 0.0027 and thickness of h = 400 µm. The conductivity has been set to $\sigma = 1.3 \cdot 10^7$ S/m considering silver ink properties. Fig. 6 shows the simulated transmission and reflection parameters of the stopband filter.

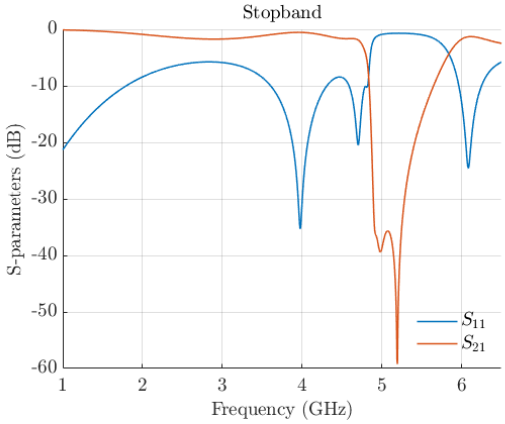


Fig. 6. Simulated S-parameters of stopband CPW filter.

The proposed filter shows a deep stopband around 5.2 GHz with maximum attenuation of 59 dB. The rejection bandwidth is wider than 1 GHz, rejection being higher than 20 dB from 4.8 GHz to 5.4 GHz. In the pass bands below and above the stopband the insertion loss remains below 2 dB.

Materials and Methods

The simulated CPW filter design has been manufactured following the AME approach. The dielectric substrate has been manufactured via FDM using ThermaX PEI filament. Two layers have been printed to obtain a h = 400 µm thick substrate with infill factor set to 100%. Lower infill values imply lower permittivity and higher loss tangent values, which reduce CPW-resonator coupling and increase passband losses, respectively. The CPW transmission lines have been screen-printed and the SRRs have been printed with micro-dispensing technique. For both printings Loctite ECI1011 silver ink has been selected due to its high conductivity.

Fig. 7 shows a picture of the manufactured stopband sample and the dimensions measured with the microscope are collected in Table 2 together with the design values to compare. In the case of the SRRs the average value corresponding to the six resonators is considered. In the case of *c* and *g*, the values for the inner (in) and outer (out) rings are presented. The actual dimensions of the rings are slightly larger compared to design due to ink spread.

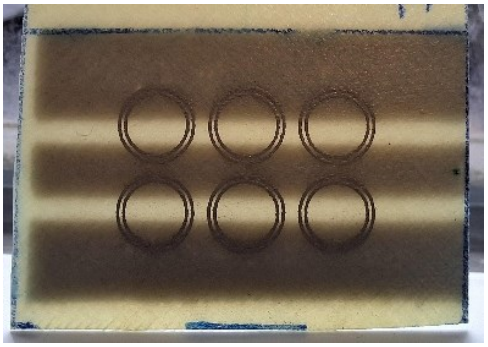


Fig. 7. Picture of manufactured AME CPW stopband filter.

Table 2. Design vs measured dimensions of manufactured AME CPW stopband filter.

Parameter	Measured	Design	**Parameter**	Measured	Design
d (µm)	197 ± 9	200	**R_{in} (mm)**	2,02 ± 0,02	2
c_{in} (µm)	220 ± 10	200	**W (mm)**	4,95	5.5
c_{out} (µm)	200 ± 10	200	**s_1 (mm)**	1	0.3
g_{in} (µm)	270 ± 70	200	**s_2 (mm)**	1	0.3
g_{out} (µm)	270 ± 50	200			

Results and Discussions

The S-parameters of the manufactured filter have been measured with a VNA between 300 kHz – 6.5 GHz. The response of the filter is shown in Fig. 8 together with the simulation and retrosimulation results. In the retrosimulation the average dimensions of the rings were considered, but the deviation and tolerances between rings were not.

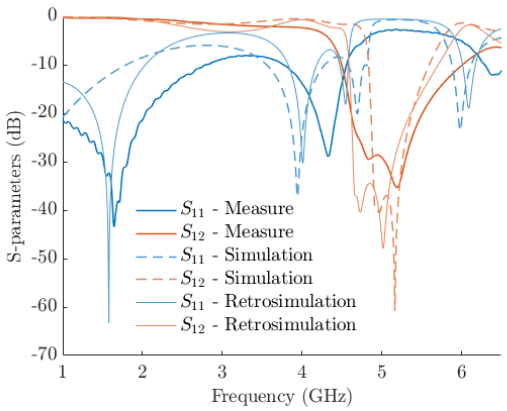


Fig. 8. Measured and simulated S-parameters for stopband CPW filters.

The stopband of the manufactured filter is centered at 5.2 GHz, in concordance with simulated results. However, the maximum obtained attenuation is 35 dB and compared to the simulated results, the bandwidth is wider, with the rejection being higher than 20 dB from 4.6 GHz to 5.5 GHz. This is due to the 1-mm width of the gaps *s* of the CPW transmission line, which were designed to be much narrower (*s* = 0.3 mm).

The insertion loss in the pass bands below and above the stopband is higher than in simulations, especially as the stopband is approached. The SRRs exhibit dimensional tolerances and although this effect has not been simulated, it may have caused slight decoupling between the resonances of each ring. Furthermore, resistive losses are likely to be greater than expected due to the quality of the printing, which is a result of the substrate roughness.

Conclusions

The feasibility of manufacturing CPW filters using the AME approach has been analysed. Although the measured performance exhibits a noticeable degradation with respect to the simulated response, these discrepancies are attributed to the surface roughness of the FDM-fabricated substrate and the dimensional tolerances inherent to the printing process. These preliminary results validate the potential of AME as a viable manufacturing approach for microwave filters. Nevertheless, further research is required to optimize the printing parameters and improve the surface finish and design reproducibility, thereby enhancing the electrical performance of the fabricated devices.

SENSORS EMBEDDED INTO COMPOSITE

Embedding sensors directly into composite laminates has emerged as an effective strategy for both process control and in-service monitoring [11]. In this context, printed electronics offer a scalable and cost-effective solution for integrating sensing capabilities with minimal impact on the space structures [12]. This section focuses on the development of printed temperature and strain sensors for integration in CFRPC. The sensors were successfully embedded into laminates and withstand autoclave processing, maintaining stable electrical performance. Thermal characterization showed a linear response up to 130°C with a sensitivity of approximately 0.5Ω/°C, while mechanical tests demonstrated a linear strain response with gauge factors around 1.6–1.7. These results highlight the potential of silver-based printed sensors for reliable in situ monitoring during composite manufacturing and structural health monitoring.

Materials and Methods

- *Substrate. Electrospun Veil Development*

Electrospinning technology was used to produce nanofibrous veils acting as substrates for printed sensors. A needle-free electrospinning system (Fig. 9) was employed to enable scalable production of uniform, large-area materials. Polyamide 6,6 (PA66) was selected due to its high thermal resistance (up to ~260°C), flexibility, and high porosity, which facilitates resin infiltration during composite manufacturing. Polymer solutions (14 wt%) in formic and acetic acid were optimized to produce homogeneous fibers.

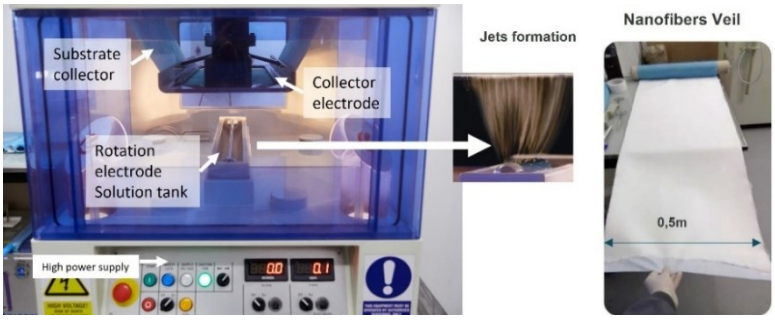


Fig. 9. Needle-free electrospinning technology.

- *Sensor Fabrication*

Sensors were fabricated using screen printing technology, with meander-shaped designs to control electrical resistance and enhance sensitivity to temperature and strain. Silver conductive ink was selected due to its high conductivity and good compatibility with the electrospun veil. Printing parameters were optimized to achieve uniform deposition and fine feature resolution (line width of 150 µm and a spacing of 200 µm between lines). After printing, a curing process at approximately 200 °C was applied to remove residual ink components and stabilize the electrical resistance of the sensors for subsequent composite manufacturing. Electrical connections were established using flexible cables to ensure reliable signal acquisition. Fig. 10 shows the design layout, the resulting printed sensors and an optical image of the silver tracks.

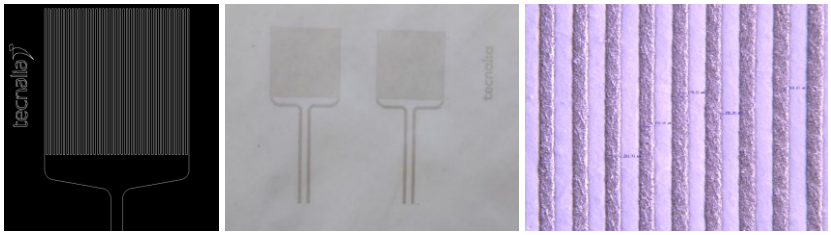


Fig. 10. Sensor design (left), Ag printed sensors on PA66 electrospun veil (centre) and optical image of the sensor tracks (right).

- *Composite Integration*

For integration, the sensors were embedded into carbon fiber prepreg laminates and cured in an autoclave. The electrospun veil acted simultaneously as a substrate and as an insulating layer, preventing electrical contact with carbon fibers and preserving sensor functionality. Fig. 11 shows the pressure and temperature conditions during the composite manufacturing process.

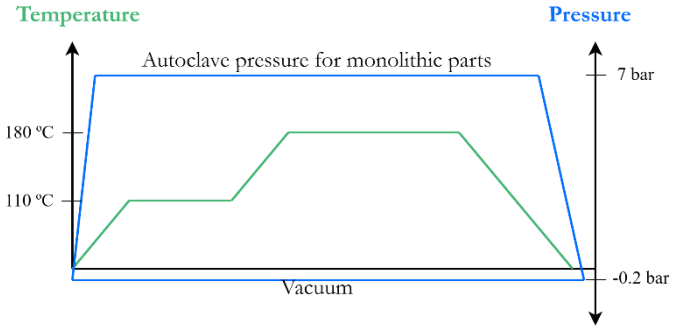


Fig. 11. Autoclave composite manufacturing process conditions.

Results and Discussion

The electrical resistance of the sensors was measured after fabrication and stabilization, followed by thermal characterization in a controlled oven where temperature cycles up to 130 ºC were applied. Mechanical characterization was performed through tensile tests according to the UNE-EN ISO527-4 standard. A commercial contact extensometer collocated in the center of the specimen was used to measure the strain. To assess the repeatability of the measurements, successive loading and unloading cycles were performed on the test specimen, reaching up to 0.5% strain.

The electrical characterization results showed that silver-based sensors exhibited resistance values typically between 130Ω and 150Ω with good reproducibility and stability. After embedding the sensors into composite laminates, it was observed that sensors maintained their electrical properties with minimal variation, confirming their robustness and compatibility with the autoclave process.

Fig. 12 shows the results of the thermal and mechanical characterization of the sensors. Thermal tests were performed under constant current, and then voltage was measured as shown in Fig. 12, obtaining R as a result. Tests revealed that silver sensors exhibited a linear relationship between resistance and temperature with a sensitivity close to 0.5Ω/ºC. Mechanical tests demonstrated that strain sensors exhibited a linear response to applied strain within the tested range, showing a gauge factor between approximately 1.6 - 1.7 and maintaining stable behavior across repeated loading cycles. These values were obtained in previous works [13].

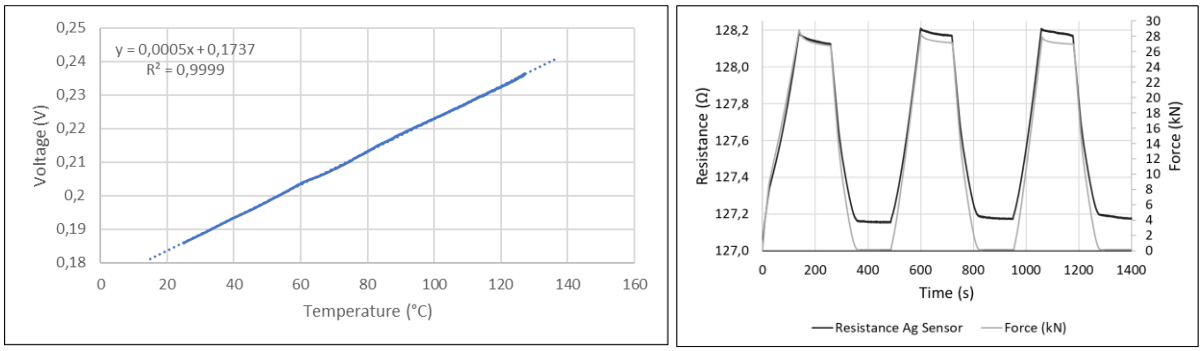


Fig. 12. Ag printed sensor performance in temperature cycles (left) and in strain cycles (right).

Conclusions

The results demonstrate the feasibility of integrating silver printed sensors on electrospun PA66 veils for structural health monitoring (SHM) applications in composite materials. The developed sensors showed good printability, excellent compatibility with autoclave processing, and stable electrical performance after embedding into composite laminates. Furthermore, the sensors exhibited a linear response to both temperature and strain, highlighting their potential for real-time monitoring of structural integrity and the development of smart composite structures with integrated sensing capabilities.

THERMALLY SELF-REGULATED COMPOSITE COMPONENT

In the electrification era, electrothermal heating, based on the Joule effect, has gained a lot of interest in the industrial field. Such systems find wide application on thermal management and de-icing systems in the automotive, aeronautical, building, and renewable energy sectors [14-16]. Ice accumulation on wings airplanes, on the car windshield or bumper, on wind turbine blades, or the roof of houses increases the weithgy of the structure [17]. Moreover, in the case of transportation means and wind turbines, the presence of ice causes a considerable change in the shape and roughness of the surface with negative effects on their stability, safeness, aerodynamics, and energy performance [18-20]. The possibility of having a heater on board directly integrated into the structure represents a huge advantage since the de-icing process could be as simple as pushing a button to remove the ice [21].
This section presents a thermally self-regulated parabolic shaped composite component consisting of a screen-printed silver-based heater and thermistor embedded into CFRPC and an electronic system designed to control composite part surface temperature. Thermal characterization showed a homogeneous surface temperature distribution through the application of 1,7 kW/m^2 by printed heater, monitored via printed sensor, and managed through electronic control. These results highlight the potential of printed heaters and sensors for reliable surface temperature control for thermal management and de-icing of composite structures.

Materials and Methods

The substrate material used for the heating element was a commercial fiberglass fabric HexForce® 02116 from HEXCEL. For the sensor an electrospun PA66 veil was used as substrate for sensor accuracy. The heating element and the sensor were screen-printed using ELANTAS BECTRON 6668 and Celanese HT-802 silver inks, respectively. After screen printing, heating and sensing elements were thermally cured. Connections for the printed heater and sensor were performed through FFC (Flat Flexible Cables) and conductive adhesive IQ-BOND 5415.

Fig. 13 shows a graphical overview of the laminating process for the integration of the different components. Concurrently, Fig. 14 is a visual depiction of the final prototype. Printed heater and sensor were laminated within prepreg fiberglass (HEXFORCE 02116) and Carbon fiber fabrics (VTC401 Epoxy Component Prepreg). VTFA400 (DF034) Epoxy Adhesive Film was used for lamination. The curing process of the laminated samples and components was performed in autoclave at 120ºC/1h and 1bar and vacuum.

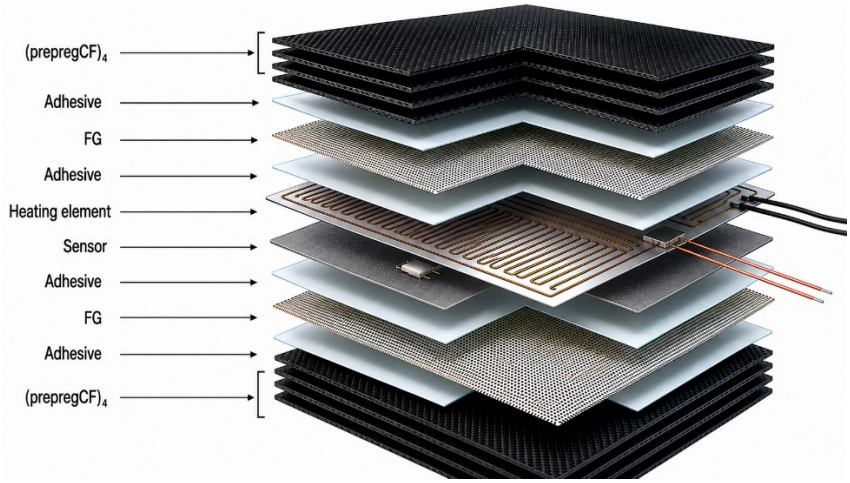


Figure 13: Layer stack-up of the embedded prototype.

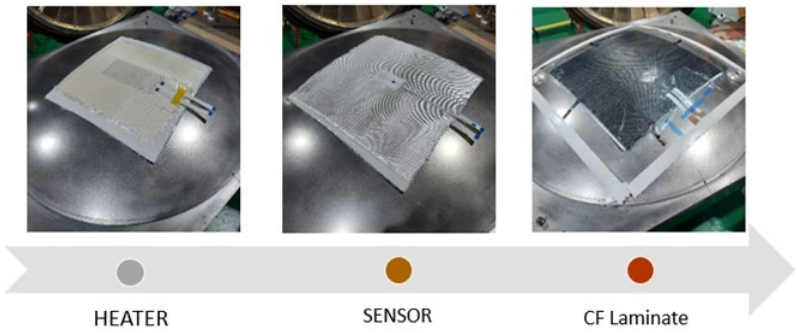


Fig. 14. Image of the lamination sequence for the embedded heating and sensing system.

Control strategy

The heating system is designed to work at 12V reaching a maximum by design of 70 ºC (for safety). The heater control strategy is based on custom-designed control electronics that manage temperature regulation using feedback from the embedded printed sensor, displaying both real-time data and the target setpoint. The system features a dedicated configuration mode, swapped via a physical switch, which allows for manual setpoint adjustment using a rotary interface. This architecture ensures precise thermal control and user-friendly parameter tuning through a localized hardware interface.

Results and discussion

- *Electrothermal Characterization*

Samples were thermoelectrically characterized before (dry) and after being embedded in the composite. For the dry characterization, samples were located in a vacuum table so that the planarity of the sample and the thermal dissipation to the table were assured while power was applied. This way, the thermal image obtained showed the heater thermal distribution with no influence of possible inhomogeneities due to uneven surface of the substrate. IR thermographic OPTRIS camera was used for surface temperature characterization and SourceMeter KEITHLEY was used for sensor electrical resistance characterization.

As collected in Table 3 no electrothermal property variation is observed for sensor or heater systems after embedding process. Fig. 15 shows the measured thermal distribution and temperature (ºC) profile of the heater along two sections (black lines on the thermal image) together with the sensor calibration curve. Homogeneous thermal distribution is assured all over the heater surface and the temperature sensor shows a linear response with good sensitivity to thermal variation.

Table 3. Electrical resistance results for heating and sensing elements before and after system embedding.

		Heating element	Sensor
Resistance (Ω)	Pre-PREPEG	6,6	222
	Post-PREPREG	6,7	221

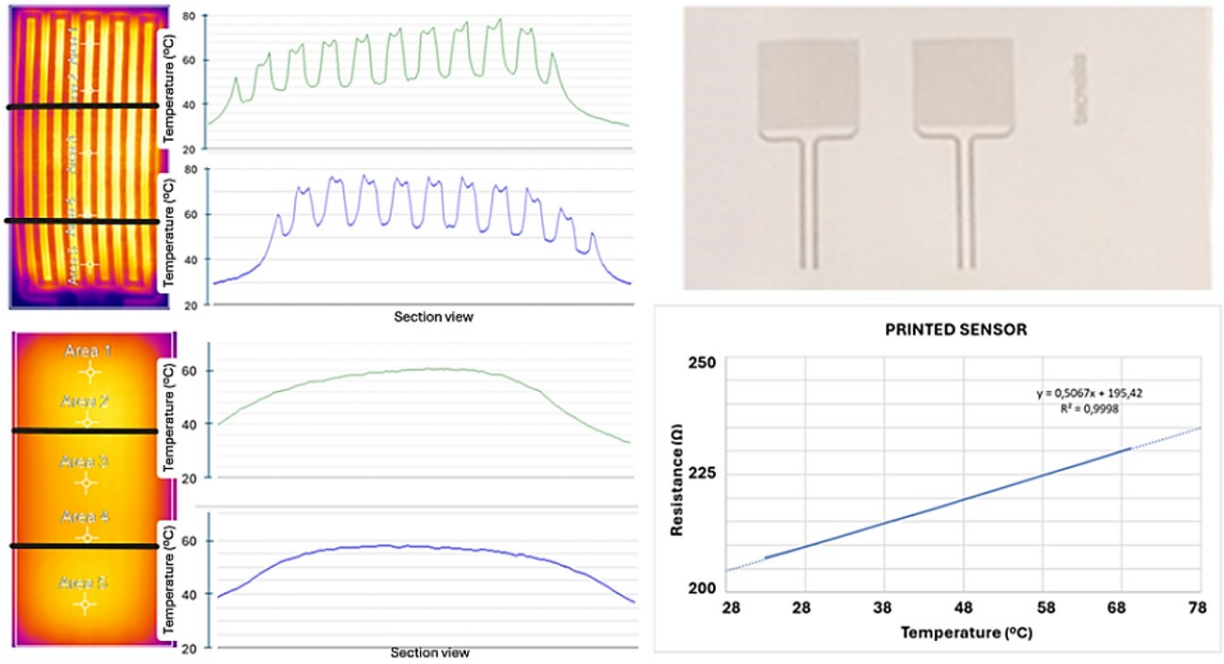


Fig. 15. Thermal image of the heating element and temperature (ºC) profile at 12V in different sections of the heater (black lines in thermal image) before (up-left) and after (bottom-left) embedding process. Image of the printed sensors (up-right) and the calibration curve showing resistance variation vs T (ºC)(bottom-right).

- *Operational validation*

For the self-regulated system validation, electronic control strategy is integrated in the system. The component performance is validated at laboratory environmental conditions. With 12 V power supply a heating power of 1,7 kW/m^2 is applied by the printed heater. The setpoint temperature is defined at the beginning and the heating power applied. Meanwhile the control system monitors the component temperature through the printed sensor controlling the heater feeding and consequently the system temperature. It is observed that the system reaches and maintains the setpoint temperature satisfactorily up to 70 ºC. Fig. 16 shows an image of the tested prototype of the thermally self-regulated parabolic shaped composite.

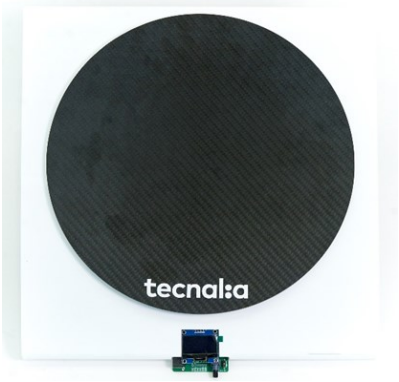


Fig. 16. Prototype of the thermally self-regulated composite.

Conclusions

A thermally self-regulated antenna (component) has been produced and validated at laboratory scale, demonstrating the feasibility of producing a completely printed self-regulating heating system.

CONCLUSIONS

This study demonstrates the viability of integrating additive manufacturing (AM) and printed electronics (PE) for next-generation space applications, effectively addressing requirements for weight reduction and architectural complexity. The fabrication of a 2.9 GHz helical antenna using Piezo ink jet printing and FDM technologies yielded a gain of approximately 4 dB and a half-power beamwidth (HPBW) of 21°, validating this workflow for critical RF subsystems. Furthermore, the development of a CPW stopband filter utilizing split-ring resonators (SRRs) exhibiting 35 dB of measured attenuation at 5.2 GHz, with rejection higher than 20 dB from 4.8 GHz to 5.4 GHz, underscores the capability to manufacture high-performance passive devices with reliable precision.

Beyond passive structures, the research establishes a robust framework for multifunctional system integration through advanced material science and sensor embedding. The utilization of thermally resistant substrates, combined with screen-printed silver inks, enabled the creation of sensitive sensor arrays exhibiting a gauge factor of 1.6–1.7 for strain monitoring and a linear sensitivity of 0.52 Ω/°C for thermal management within composite environments. Additionally, a completely printed system, combining heater (for actuation), sensor (for monitoring) and electronic system (for system functioning) has been embedded showing reliable surface temperature control. Furthermore, the demonstrated lamination sequence, involving conductive epoxy films and embedded printed elements, highlights the feasibility of lightweight, integrated thermal management systems, capable of operating in harsh orbital conditions.

Collectively, these findings confirm that additively manufactured and printed electronic systems can be reliably adapted for space-grade environments, offering significant advantages in weight reduction, design flexibility, and rapid prototyping. This work establishes a foundational framework for the widespread adoption of integrated printed electronics in future missions, paving the way for more autonomous, cost-effective, and highly integrated satellite architectures.

REFERENCES

[1] Rao, C. H., Avinash, K., Varaprasad, B. K. S. V. L., & Goel, S. (2022). A Review on Printed Electronics with Digital 3D Printing: Fabrication Techniques, Materials, Challenges and Future Opportunities: CH Rao et al. *Journal of Electronic Materials*, *51*(6), 2747-2765.

[2] Wiklund, J., Karakoç, A., Palko, T., Yiğitler, H., Ruttik, K., Jäntti, R., & Paltakari, J. (2021). A review on printed electronics: fabrication methods, inks, substrates, applications and environmental impacts. *Journal of Manufacturing and Materials Processing*, *5*(3), 89.

[3] Maalderink, H. H., Bruning, F. B., De Schipper, M. M., Van Der Werff, J. J., Germs, W. W., Remmers, J. J., & Meinders, E. R. (2018). 3D Printed structural electronics: embedding and connecting electronic components into freeform electronic devices. *Plastics, Rubber and Composites*, *47*(1), 35-41.

[4] Beneventi, D., Graziano, A., Furia, G., Charpin, L., & Jean-Louis, M. (2023). Optimization of trajectory processing algorithms to print 3D circuit boards using piezo ink jet and 6-axis robots. *Journal of Manufacturing Processes*, *101*, 1497-1507.

[5] A. Pérez-Márquez, J. Maudes, L. Bilbao, C. Vaquero, H. Villaverde, O. Adarraga, I. Bustero, I. Obieta, and J. Gayoso, “Mechanical properties analysis of continuous fiber composites with embedded printed electronics.” In Materiales Compuestos, 2022.

[6] Sacco, E., & Moon, S. K. (2019). Additive manufacturing for space: status and promises. *The International Journal of Advanced Manufacturing Technology*, *105*(10), 4123-4146.

[7] Kraus, J. D. (2006). The helical antenna. *Proceedings of the IRE*, *37*(3), 263-272.

[8] Friis, H. T. (1946). A note on a simple transmission formula. *proc. IRE*, *34*(5), 254-256.

[9] Martin, F., Falcone, F., Bonache, J., Marqués, R., & Sorolla, M. (2003). Miniaturized coplanar waveguide stop band filters based on multiple tuned split ring resonators. *IEEE microwave and wireless components letters*, *13*(12), 511-513.

[10] Certified Material Ultem 9085 - STRATASYS GMBH - PDF Catalogs | Technical Documentation | Brochure

[11] Zhao, D., Liu, X., Meves, J., Billings, C., & Liu, Y. (2023). 3D printed and embedded strain sensors in structural composites for loading monitoring and damage diagnostics. *Journal of Composites Science*, *7*(10), 437.

[12] Nauman, S., Asfar, Z., Ahmed, S., Nasir, M. A., & Hocine, N. A. (2023). On the in-situ on-line structural health monitoring of composites using screen-printed sensors. *Journal of Thermoplastic Composite Materials*, *36*(1), 234-252.
[13] A. Perez-Marquez, M. Puerto-Coy, P. Casado and J. Mendikute, "Functional printing for main distortion points in cured composite parts," *2024 39th Conference on Design of Circuits and Integrated Systems (DCIS)*, Catania, Italy, 2024, pp. 1-6, doi: 10.1109/DCIS62603.2024.10769189.
[14] Tinti, A., Carallo, G. A., Greco, A., Romero-Sánchez, M. D., Vertuccio, L., & Guadagno, L. (2022). Effective practical solutions for de-icing of automotive component. *Nanomaterials*, *12*(17), 2979.
[15] Guo, X., Yang, Q., Zheng, H., & Dong, W. (2024). Integrated composite electrothermal de-icing system based on ultra-thin flexible heating film. *Applied Thermal Engineering*, *236*, 121723.
[16] Wei, K., Yang, Y., Zuo, H., & Zhong, D. (2020). A review on ice detection technology and ice elimination technology for wind turbine. *Wind Energy*, *23*(3), 433-457.
[17] Borrebaek, P. O. A., Jelle, B. P., & Zhang, Z. (2020). Avoiding snow and ice accretion on building integrated photovoltaics–challenges, strategies, and opportunities. *Solar Energy Materials and Solar Cells*, *206*, 110306.
[18] Gao, L., Tao, T., Liu, Y., & Hu, H. (2021). A field study of ice accretion and its effects on the power production of utility-scale wind turbines. *Renewable energy*, *167*, 917-928.
[19] Wu, Z., & Wang, Q. (2020). Effect of and protection from ice accretion on aircraft. *Ice Adhesion: Mechanism, Measurement and Mitigation*, 577-606.
[20] Prasad, G. (2020). Experimental and computational study of ice accretion effects on aerodynamic performance. *Aircraft Engineering and Aerospace Technology*, *92*(6), 827-836.
[21] Aliberti, F., Sorrentino, A., Palmieri, B., Vertuccio, L., De Tommaso, G., Pantani, R., ... & Martone, A. (2024). Lightweight 3D-printed heaters: design and applicative versatility. *Composites Part C: Open Access*,*15*, 100527.